

Biomimetic Flexible High-Sensitivity Near-Infrared II Organic Photodetector for Photon Detection and Imaging

Yingjun Xia, Chen Geng, Xingqi Bi, Mingpeng Li, Yu Zhu, Zhaoyang Yao,* Xiangjian Wan, Guanghui Li,* and Yongsheng Chen

The flexible near-infrared (NIR) organic photodetector is an essential prerequisite for the next-generation visual system for accurate information identification. However, prevailing limitations in NIR organic photodetectors, including high noise, weak responsivity, and low detectivity, directly impede the translation to practical applications. Herein, ultranarrow bandgap acceptors, featuring a 2D highly electron-donating central core (DTPC), named as YZ and YZ1, are designed and synthesized for NIR organic photodetectors. It is found that the introduction of highly rigid DTPC effectively reduces energetic disorder in active films. Moreover, extending the end conjugation not only broadens the absorption spectrum but also diminishes trap states and improves charge transport. Consequently, the YZ1-based organic photodetector exhibits an impressive detection range from 300 to 1050 nm with a high responsivity of 0.27 A W⁻¹ at 1000 nm and specific detectivity of 9.24×10^{13} Jones, comparable to commercial silicon photodiodes. Inspired by biological eyes, large-area parallelly independent photodetector arrays (2000 pixels) for an artificial vision system are fabricated, which enables a clear matter identification in the NIR region. These findings and results simultaneously provide critical insights into molecular design and bridge the gap between material science and device engineering, accelerating the application of NIR organic photodetectors in next-generation wearable optoelectronics.

external environment.^[1–3] Artificial vision systems, such as artificial retinas and wearable visual systems for the blind or eye repair, composed of flexible, large-area, high-density, and highly sensitive photodetector arrays, have distinct advantages, including lightweight, wide field of view (FOV), and active adaptability to complex geometries and optical systems.^[3–7] In particular, flexible near-infrared II (NIR-II, $\lambda > 1000$ nm) photodetectors beyond the human visual spectrum, to a large extent, have emerged as indispensable components in both research and industrial applications, such as biological detection, wellness monitoring, night-vision imaging, machine vision, and optical communication.^[8–10] Even though state-of-the-art NIR photodetectors based on single-crystalline inorganic semiconductors exhibit remarkable performance, their fabrication typically involves high-temperature, complex microfabrication process, and sophisticated techniques. Additionally, these traditional inorganic NIR photodetectors generally suffer from mechanical rigidity, small size, and inferior spectrum selectivity, limiting their applications in emerging fields that demand large-area and flexible

NIR photodetector arrays.^[11–13] Moreover, commercial inorganic infrared photodetectors/imagers usually require active cooling to mitigate thermal noise, resulting in high power consumption.^[13,14] An elegant strategy to circumvent these limitations is thin-film organic photodetectors (OPDs) with bulk heterojunction (BHJ) structure, which have demonstrated superior performance over commercial silicon photodetectors in various key metrics.^[8,15,16] Moreover, inherent advantages of OPDs, including intrinsic merits of flexibility, tailorable spectral detection, ease of solution processing, and biocompatibility, make OPDs as ideal candidates for the next-generation artificial visual systems.^[17–19]

Benefiting from in-depth investigations in organic photovoltaic materials, particularly the non-fullerene acceptors (NFAs) featuring an acceptor-donor-acceptor (A-D-A) architecture,^[20] such as CO1-4Cl,^[9] PDDTTIC-4F,^[21] COi8DFIC,^[22] COTIC-4F,^[14,23,24] OPDs have achieved tremendous advances in visible to near-infrared (vis–NIR) detection with remarkable optoelectronic performance.^[25] Despite extensive studies have been conducted to extend the π -conjugated length of the central core unit in the

1. Introduction

Human eyes are undoubtedly the dominant sensory organ that acquires more than 80% of information from the complex

Y. Xia, C. Geng, X. Bi, M. Li, Y. Zhu, Z. Yao, X. Wan, G. Li, Y. Chen
The Centre of Nanoscale Science and Technology and Key Laboratory of Functional Polymer Materials
Institute of Polymer Chemistry
Renewable Energy Conversion and Storage Center (RECAST)
College of Chemistry
Nankai University
Tianjin 300071, China
E-mail: zyao@nankai.edu.cn; ghli1127@nankai.edu.cn

Y. Chen
State Key Laboratory of Elemento-Organic Chemistry
Nankai University
Tianjin 300071, China

 The ORCID identification number(s) for the author(s) of this article can be found under <https://doi.org/10.1002/adom.202301518>

DOI: 10.1002/adom.202301518

1D direction, it remains a formidable challenge to construct ultranarrow bandgap NFAs with frontier molecular orbitals that align well with current donors for high-sensitivity NIR OPDs. On the one hand, the upshifted highest occupied molecular orbitals (HOMOs) of narrowband NFAs generally cause poor exciton dissociation, while the downshifted lowest unoccupied molecular orbitals (LUMOs) decrease the effective bandgap and lead to high noise current.^[14,25–27] Furthermore, the inherently disordered microstructure due to the imperfect molecular packing unavoidably causes high energetic disorder and trap states, where broad electronic states in active films reduce the barrier to thermally excited charges and trap states facilitate the charge excitation from donor HOMOs to acceptor LUMOs, leading to high noise current in NIR OPDs.^[8,22,26–28] More recently, experimental and theoretical investigations have revealed that extending central cores of NFAs in a 2D direction can efficiently enlarge the conjugation length of central cores, enhance inter- and/or intramolecular packing, and suppress molecular vibrations or torsions, ultimately broadening optical absorption and reducing molecular disorder and trap states.^[29–32] Additionally, extending end conjugation of NFAs promotes intermolecular π - π overlaps, enhances the intramolecular charge transfer (ICT) effect, and improves end-to-end molecular packing, which broadens spectral absorption and improves charge mobility.^[29,30] With these thoughts in mind, we believe that it is essential to design ultranarrow bandgap NFAs with appropriate frontier molecular orbitals and molecular packing by simultaneously extending the central cores in 2D directions and enlarging end conjugation length to reduce energetic disorder and trap states for high-performance photon detection and imaging. Furthermore, designing and developing large-area, high-density flexible OPD arrays can significantly improve imaging quality and eliminate the need for bulky 2D translation stages typically employed in single OPD pixel imaging, which holds great potential to expand the practical applications in artificial vision systems.^[8,22]

Here, we report a rational material design and a straightforward device fabrication strategy for developing high-performance biomimetic flexible NIR-II OPD arrays utilized in photon detection and imaging. Our approach involves incorporating a highly electron-donating and rigid 2D central unit, 9,14-dihydro-4*H*-dithieno [2',3':2,3;3'',2'':10,11]piceno[1,14,13,12-*bcdefgh*]carbazole (DTPC), for constructing narrow-bandgap NFAs named as YZ and YZ1, which are terminated with 2-(3-oxo-2,3-dihydro-1*H*-inden-1-ylidene)malononitrile (INCN-2F) and 2-(6,7-difluoro-3-oxo-2,3-dihydro-1*H*-cyclopenta[*b*]naphthalen-1-ylidene) malononitrile (NINCN-2F) as end electron-withdrawing units, respectively. Notably, both YZ and YZ1 acceptors demonstrate broad optical absorption from visible to NIR region and extremely low energetic disorder in blend films. Moreover, compared with YZ NFA, the YZ1 NFA with a larger conjugation end group (NINCN-2F) not only shows broader optical absorption range from 300 to 1050 nm, but also demonstrates lower trap states and higher charge mobility, significantly suppressing noise current and boosting charge transport. Consequently, the optimal OPD based on YZ1 demonstrates outstanding optoelectronic performance comparable to that of commercial silicon photodetectors in the NIR-II region and ranks one of the highest values reported in this spectral range. Particularly, the NIR-II OPD exhibits high responsivity (0.27 A W^{-1} at

1000 nm), high specific detectivity (over 10^{13} Jones), and rapid photoresponse (976/600 ns). Moreover, the corresponding flexible OPD retains 99.9% of its initial outstanding photoresponse after bending for 100 cycles. Inspired by the architecture of biological eyes, we designed large-area high-density flexible OPD arrays that could integrate with commercial eyeglasses for artificial vision, which demonstrated a clear target imaging in the NIR region. Our high-performance flexible NIR-II OPD array paves a new way to develop novel artificial visual systems applied in emerging fields where conventional inorganic photodetectors fall short, such as artificial retinas, soft machine vision, and lightweight night-vision systems for multifunctional applications.

2. Results and Discussion

2.1. Optoelectronic Performance of NIR-II OPDs

The human eye, composed of a lens, spherical cavity, and hemispherical retina, is the core component of visual system, which converts incident light into neuroelectric signals and then transmits to the brain for data processing (Figure 1a-i).^[1,3] There are approximately 100–200 million cones rods cells⁻¹ (Figure 1a-ii) that parallelly and vertically assemble in the retina to convert light into electrical signals, which is similar to the architecture of our flexible OPD array (Figure 1a-iii). Very recently, we reported an ultranarrow bandgap NFA based on the highly rigid 2D DTPC central unit terminated with INCN-2F (YZ, Figure 1b-i), which exhibited a narrow optical bandgap of 1.26 eV and demonstrated a strong absorption in the NIR region, with an onset spectra absorption of 984 nm.^[32] Even though the YZ-based organic photovoltaic device shows outstanding external quantum efficiency (EQE), it still lags behind commercial silicon photodiodes in the NIR region.^[32] Therefore, our molecular design aims to achieve NFAs with ultranarrow bandgaps, suitable frontier molecular orbitals, and well molecular packing to construct high-performance NIR OPDs above 1000 nm.

Here, we introduced a highly electron-deficient end group of NINCN-2F to further extend its conjugation length and enhance the intramolecular charge transfer (ICT) effect (Figure 1b-ii). In comparison with YZ NFA, the resulting YZ1 NFA film exhibited primary absorption from 600 to 1050 nm and peaked at 921 nm, with a negligible change of LOMO, thereby maintaining the effective bandgap of the OPD (Table S1, Supporting Information). Here, we selected an inverted structure of OPD and chose ZnO as the electron transport layer due to its efficient suppression of dark current density and noise.^[21] PCE-10 (Figure 1b-iii) was selected as the donor due to its complementary spectrum and well-matched energy level with YZ1 and YZ NFAs (Figure 1c–e). More details of materials synthesis, device fabrication, and characterizations can be found in Supporting Information. Inspired by the biological visual system, we conceived the concept of a wearable vision system based on a high-resolution flexible OPD array for NIR imaging (Figure 1f).

Analogous to the biological rods/cone cells in the retina, OPDs operating in the self-powered mode convert light into micro-nano current pulses at 0 V bias voltage. These pulsing signals are subsequently processed and transmitted to the brain through

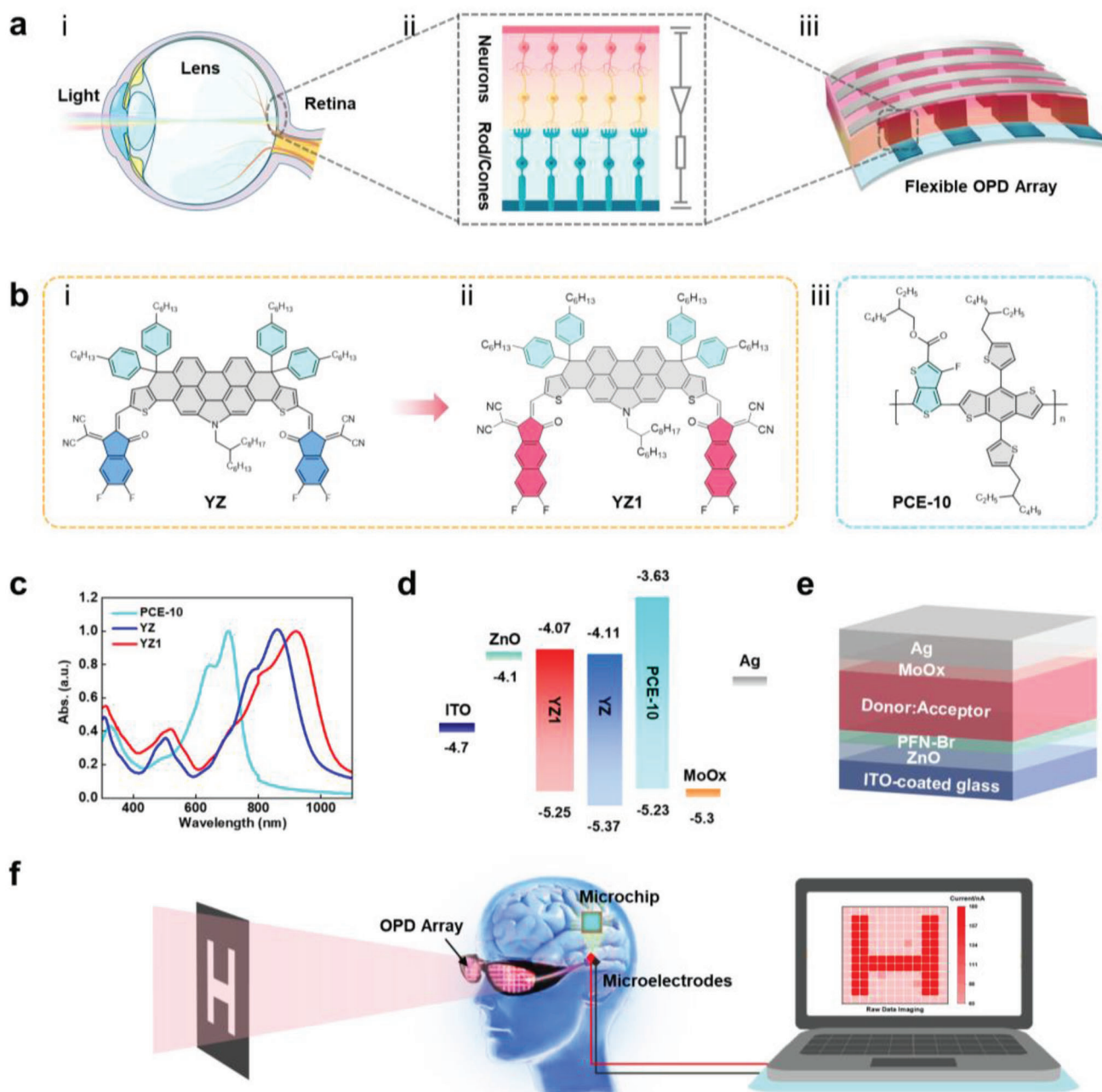


Figure 1. a–iii) Schematic of a biological eye, mechanism of retina function, and flexible high-density OPD array. b–iii) Chemical structures of YZ, YZ1, and PCE-10. c) Normalized thin film absorption spectra of PCE-10, YZ, and YZ1. d) Energy diagram. e) Schematic of device structure. f) Schematic of wearable vision system with flexible OPD arrays and the procedure of imaging.

microelectrode arrays for imaging perception (Figure 2a).^[1] Therefore, the optoelectronic performance of self-powered OPDs, including responsivity, noise, and response speed, primarily determines the imaging quality of the artificial visual system. At 0 V bias voltage, the YZ-based OPD demonstrates an ultra-low dark current density of 0.84 nA cm^{-2} , while the YZ1-based OPD exhibits a remarkably lower dark current density of 0.053 nA cm^{-2} with an ideal factor of 1.63 close to 2 as predicted by the non-ideal generalized Schokley diode equation (Figure 2b; Table S2, Supporting Information).^[14,27,33] This suggests that

trap-assisted recombination dominates the dark current density in YZ1-based devices. Furthermore, the YZ1-based OPD exhibits a broadband and distinct photoresponse ranging from 300 to 1050 nm, with a high responsivity of 0.27 A W^{-1} at 1000 nm, which surpasses both the YZ-based OPD (0.07 A W^{-1}) and popular commercial silicon photodetectors, ensuring its applications in the visual system for high-quality NIR imaging (Figure 2c; Figure S5, Supporting Information).

Noise (S_n), the key factor that affects the quality of imaging, is composed of shot noise (S_{sh} , determined by J_d), thermal noise

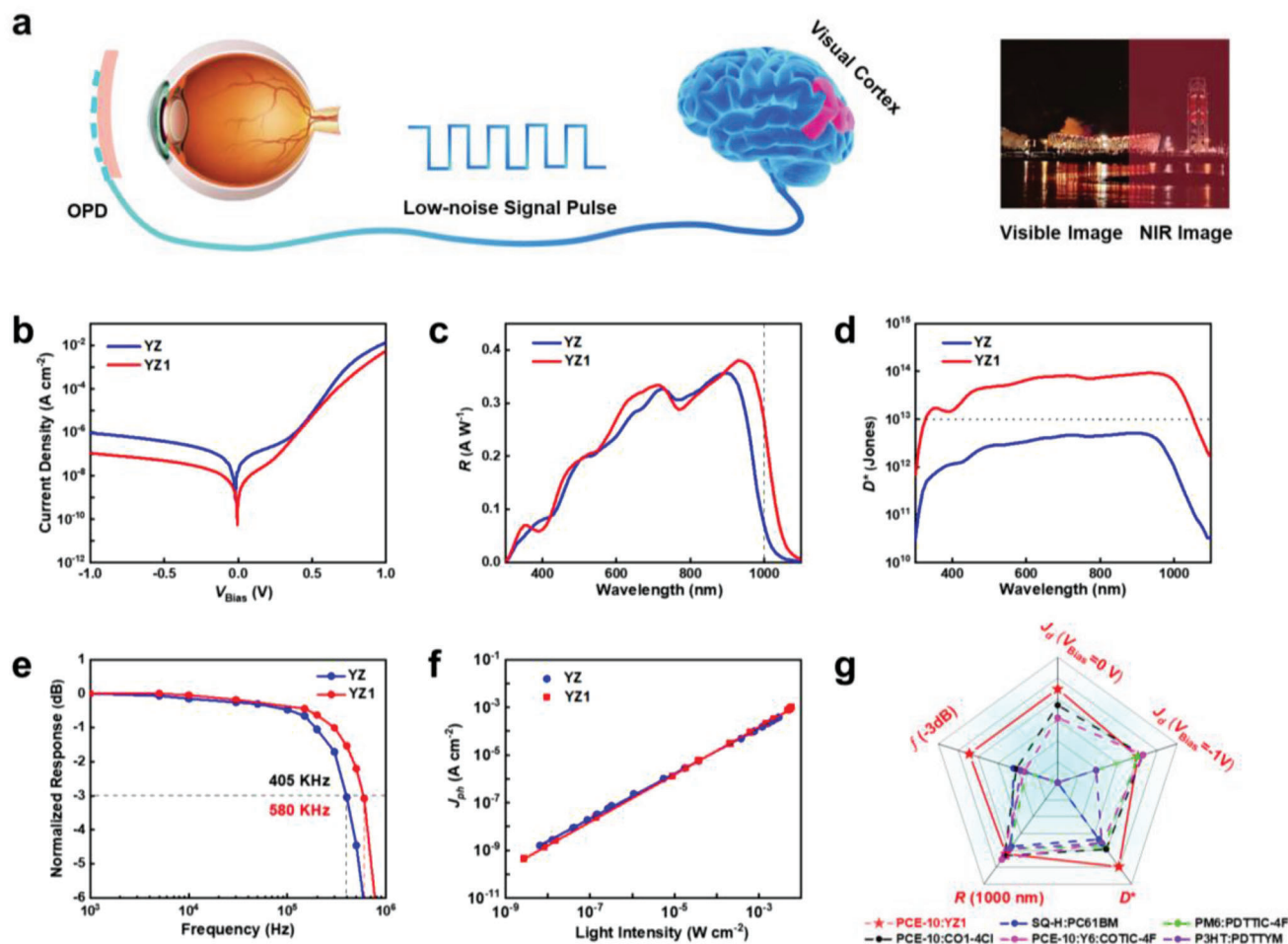


Figure 2. Characterizations of OPDs based on YZ and YZ1 acceptors. a) Imaging process of wearable optoelectronics. b) J - V curves in the dark. c) Responsivities of OPDs working at 0 V bias voltage. d) Specific detectivities of OPDs at 0 V bias voltage. e) -3 dB cutoff frequency under 905 nm illumination. f) The measured (dot) and fitting (line) linear dynamic range under 905 nm illumination. g) Major parameters comparison of the YZ1-based OPD and previously reported NIR OPDs.

(S_{th} , limited by R_{sh} and T), and flicker noise (S_f), which is described as following^[19,34]

$$S_n = \sqrt{(S_{sh}^2 + S_{th}^2 + S_f^2)} = \sqrt{\left(2qJ_d + \frac{4kT}{R_{sh}} + S_f^2\right)} \quad (1)$$

In the NIR OPD, the shot noise is the main source and independent of frequency, which is determined by the dark current density.^[27,35] The shot-noise-limited specific detectivity (D^*) is extracted by combining responsivity and dark current density described by

$$D^* = \frac{R}{\sqrt{2qJ_d}} \quad (2)$$

where the YZ1-based OPD achieves values over 10^{13} Jones from 300 to 1000 nm attributed to its high photoresponsivity and relatively low dark current density, surpassing that of the YZ-based OPD (over 10^{12} Jones) and ranking among the highest reported

values in the literature of NIR OPDs (Figure 2d). To prevent performance overestimation, here the noise spectral density (S_n) of the YZ1-based OPD is probed by the fast Fourier transform of dark current density at 0 V bias voltage, exhibiting an extremely low total noise (S_n) of 5.74×10^{-15} A Hz^{-1/2} at 10 Hz, corresponding to a specific detection of 1.4×10^{13} Jones (Figure S6, Supporting Information).

To authentically mimic the working process of the biological eye, the photoresponse of the OPD is evaluated under pulsatile illumination of 905 nm in the self-powered mode, showing a stable and fast dynamic photoresponse (Figure S7, Supporting Information). In addition to detectivity, the response and recovery time of OPDs, defined as the time it takes to rise from 10% to 90% of the steady-state values, are other important parameters to evaluate the performance of OPDs. As shown in Figure S8 (Supporting Information), the YZ1-based OPD exhibits a short response time/recovery time of 976 ns/600 ns, which is considerably faster than those of the YZ-based OPD (1520 ns/1770 ns) and previous NIR OPDs, largely exceeding the response time of the human eye (40–150 ms) and the imaging frame time (33 ms).^[1,36,37]

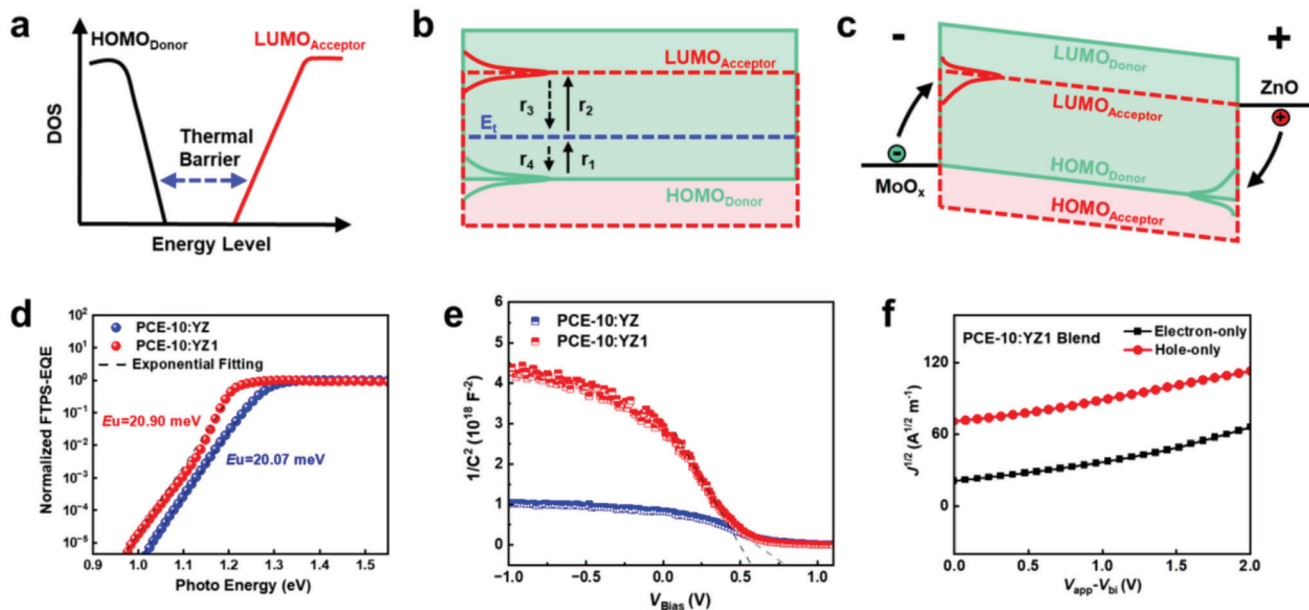


Figure 3. Working mechanism of OPDs. a–c) Dark current generation process of OPD in the self-powered mode and at reverse bias voltage. d) Urbach energy of the BHJ blend films. e) Mott–Shockley plots (dashed lines represent the linear fitting). f) Charge mobilities of the BHJ blend film.

Consistent with the response time, the YZ1-based OPD also demonstrates a higher -3 dB cutoff frequency (580 kHz), demonstrating a broader bandwidth of applicability compared to the YZ-based device (405 kHz) shown in Figure 2e. It is worth noting that the YZ1-based device shows an even faster response in the visible range, with a response time of 420 ns and a recovery time of 435 ns, as well as a -3 dB cutoff frequency of 1.3 MHz, at 700 nm (Figure S9, Supporting Information).

The broad visual adaptation ability of biological or artificial eyes allows for perception and recognition of objects under a wide range of illumination intensities, from extremely dark to bright environments. This ability heavily relies on the responsivity and noise characteristics of photoreceptors/OPDs. As shown in Figure 2f, the YZ1-based OPD demonstrates an excellent linear dynamic range (LDR) of 127 dB, surpassing that of the YZ-based OPD (104 dB), popular image sensors using silicon complementary metal-oxide-semiconductors (70 dB), and the human eyes (40 dB)^[3,38] (Table S3, Supporting Information). To the best of our knowledge, the YZ1-based OPD exhibits state-of-the-art optoelectronic performance across all relevant metrics for self-powered OPDs in the NIR-II region, including responsivity (R), -3 dB cutoff frequency ($f_{-3\text{ dB}}$), dark current density (J_d), and specific detectivity (D^*), as shown in Figure 2g and Table S4 (Supporting Information).

2.2. Energetic Disorder and Trap States Characterizations

As discussed above, in NIR OPDs operating in photovoltaic mode, thermally excited charges are the dominant noise current, which is primarily correlated to effective bandgap (E_{CT}),^[35,39] trap states,^[26,27] and energetic disorders^[35] in organic materials and devices. In BHJ OPDs that consist of donor and acceptor materials, the effective bandgap is determined by the difference between

the highest occupied molecular orbital (HOMO) of the donor and the lowest unoccupied molecular orbital (LUMO) of the acceptor. Organic semiconductors have a wide energy state distribution extending into the bandgap and forming band tail states, where a low concentration of thermally generated carriers occupies the lowest energy states far from the band edges. As a result, the effective barriers to thermally generated charges decrease with the increase of energy state distribution, leading to an increasing free charge and noise current (Figure 3a).^[35] Another factor contributing to the dark noise current is the presence of mid-gap traps in the BHJ blend, which are involved in charge generation and recombination.^[27,39] According to the Shockley–Read–Hall (SRH) theory,^[40] an electron is thermally excited from the donor HOMO (CT ground state) to a trap state (r_1) located in the middle of the bandgap. This is followed by a second excitation and further release to the acceptor LUMO (r_2), contributing to the concentration of thermally excited charges (Figure 3b).^[41–43] In this thermal charge generation and recombination process, the trap center occupied by a hole (or electron) may recombine with an electron (or hole) from the acceptor LUMO (or donor HOMO) or emit to the donor HOMO (or acceptor LUMO) until equilibrium is reached by equal capture and emission rates for holes and electrons.^[35,40] Accordingly, the thermal charge generation increases linearly with the concentration of trap states, therefore, higher concentration of trap states generally result in the higher dark noise current.^[26] At reverse bias voltage, electrons (or holes) are injected from the anode (or cathode) into the LUMO (or HOMO) tail states of donors (or acceptors), resulting in an increasing dark current with the magnitude of the reverse voltage (Figure 3c).^[26] Therefore, reducing energetic disorder and trap states can effectively suppress the generation of thermally excited charges in the organic film, thereby reducing the noise current.^[26,27,35]

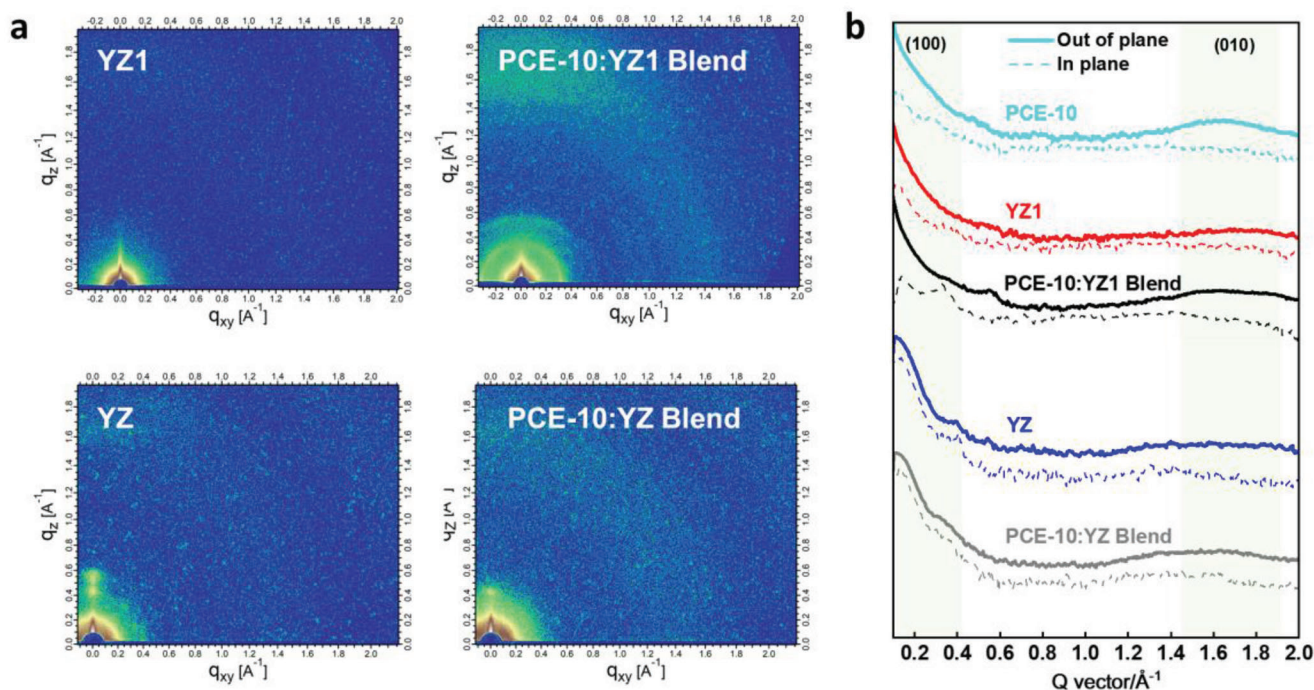


Figure 4. GIWAXS of YZ and YZ1 films. a) 2D GIWAXS patterns of YZ, YZ1, PCE-10:YZ, and PCE-10:YZ1 blend film. b) Corresponding 1D line cuts.

With these thoughts in mind, we first quantify the energetic disorder of the BHJ blend films by introducing Urbach Energy (E_U), which describes the width of the tails of the electronic density of states (DOS) and reflects the degree of overall energetic disorder.^[29,44] Remarkably, the YZ-based OPD exhibits extremely low E_U values of 20.07 meV, which is one of the lowest values ever reported for the same type of device (Figure 3d; Table S5, Supporting Information). Additionally, the YZ1 with a larger conjugation end unit shows a similar E_U with YZ in the blend film. This indicates that the introduction of highly rigid 2D central core unit in NFAs effectively reduces energetic disorder, thus increasing the barrier to thermally excited charges. To investigate the trap states in the optimized devices, capacitance–voltage (C – V) measurements were conducted (Supporting Information). The trap density of the YZ-based OPD is as low as $1.54 \times 10^{16} \text{ cm}^{-3}$ to the Mott–Shockley analysis at various bias voltages. In comparison, the YZ1-based OPD exhibits a significantly lower trap density of $4.24 \times 10^{15} \text{ cm}^{-3}$, which is one of the lowest values ever reported in binary OPDs (Figure 3e; Figure S10 and Table S6, Supporting Information). As a result, it is difficult for thermally excited charges to transit from the edge of donor HOMO to acceptor LUMO without the involvement of trap states, leading to low concentration of free charges and low noise current.^[14] According to the results of capacitance–voltage (C – V) measurements shown in Figure 3e, the YZ1-based OPD shows a large depletion width (213 nm) at 0 V bias voltage, which exceeds the thickness of the BHJ sensing layers (110 nm). This indicates that the total sensing layer is fully depleted at 0 V bias voltage, enhancing the efficient separation of charges and improving the external quantum efficiency. The YZ1-based OPD demonstrates high hole and electron mobilities of 3.67×10^{-4} and $3.84 \times 10^{-4} \text{ cm}^2 \text{ V}^{-1} \text{ s}^{-1}$, respectively, with a balanced mobility ratio of 0.96 close to the ideal values, en-

suring efficient and rapid charge transport in the BHJ blend film (Figure 3f; Table S7, Supporting Information). Theoretically, the transit time of electrons and holes can be calculated according to

$$\tau_{e,h} = \frac{d^2}{\mu_{e,h} V_{bi}} \quad (3)$$

where $\tau_{e,h}$ is the transit time, d is the film thickness, μ is the carrier mobility, and V_{bi} is the built-in voltage of the device. The theoretical value of the transit time is ≈ 600 ns, which is rather close to the experimental data.

2.3. Film Morphology Analysis

The combination of theoretical and experimental studies has demonstrated that A-D-A type molecules with enhanced planarity and rigidity in their π -conjugated backbones generally exhibited ordered molecular packing, reduced electron-vibration coupling, low energetic disorder, and fewer trap states.^[28,32,45] To further understand the reasons behind low trap states and energetic disorder of YZ and YZ1-based OPDs, grazing-incidence wide-angle X-ray scattering (GIWAXS) and atomic force microscopy (AFM) were, thus, implemented to investigate the morphology of PCE-10:YZ1 and PCE-10:YZ BHJ blends (Supporting Information). As shown in Figure 4, both YZ and YZ1 exhibit a preferential face-on orientation relative to the substrate with clear π – π stacking (010) peaks in the out-of-plane (OOP) direction and lamellar stacking (100) peaks in the in-plane (IP) direction. Table S8 (Supporting Information) summarizes peak positions, stacking distance (d), and crystal coherence lengths (CCL) of blend films prepared by PCE-10:YZ1 and PCE-10:YZ. Compared with YZ blend

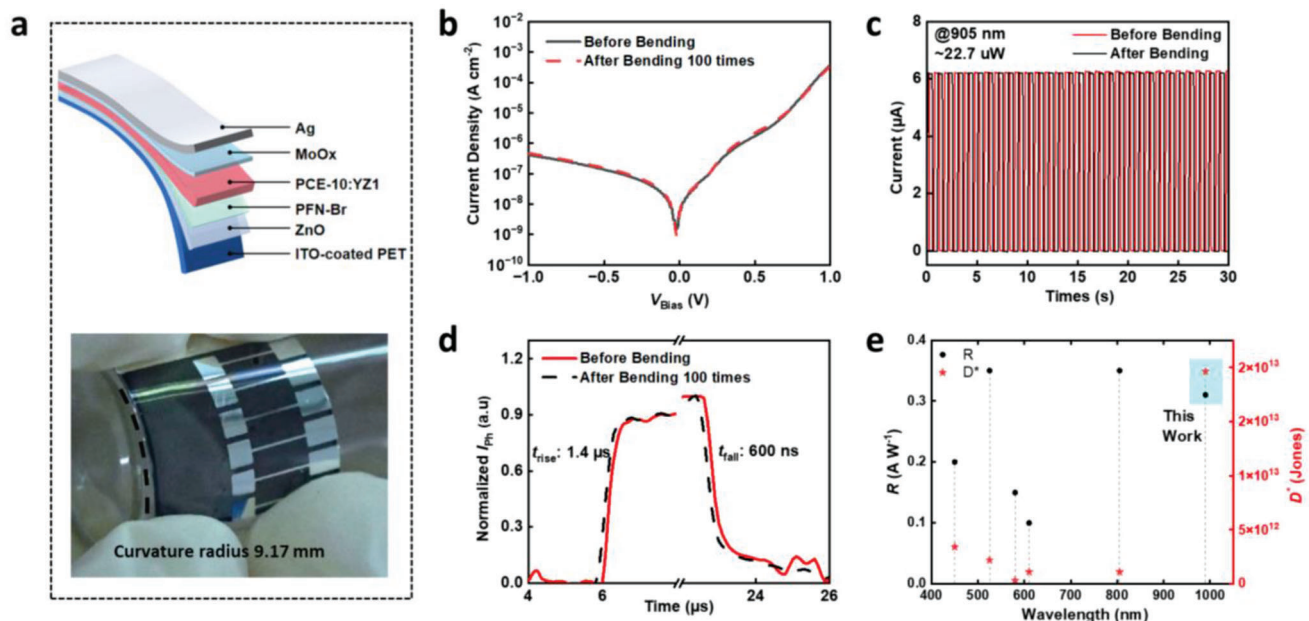


Figure 5. Optoelectronic performance of flexible NIR-II OPD. a) Schematic of flexible NIR-II OPD and its corresponding optical picture under bending. b) J - V curves of the flexible device before and after bending 100 times. c) Photoresponse of the flexible device before and after bending 100 times. d) Response and recovery time of flexible device before and after bending 100 times. e) Summary of flexible NIR OPDs key parameters.

with a d-spacing of 3.83 Å in the out-of-plane direction, the YZ1 blend shows a shorter d-spacing of 3.72 Å, indicating a more ordered molecular packing. Furthermore, the π - π stacking CCL increased from 13.58 Å (PCE-10:YZ blend) to 20.37 Å (PCE-10:YZ1 blend) by introducing larger end groups, which indicates that larger crystalline domains may form in the blend film of PCE-10:YZ1. Therefore, proper structure change can lead to more ordered molecular stacking and larger domain size, thus promoting charge transport in the vertical direction. Moreover, the root mean square (RMS) roughness of the YZ1 blend was measured to be 2.42 nm, much thinner than the total thickness of the blend (110 nm), which is beneficial for reducing shunt leakage related to nonuniformity of interfaces (Figure S11, Supporting Information). These results contribute to the low dark current density and fast photoresponse in the OPDs.

2.4. Optoelectronic Performance of Flexible NIR-II OPD

High-performance flexible NIR-II OPDs are core components of wearable visual systems. Benefiting from the intrinsic flexibility of organic materials, flexible YZ1-based NIR-II OPDs constructed on flexible ITO/PET substrates exhibit excellent electronic performance and mechanical flexibility (Figure 5a). Specifically, the flexible YZ1-based NIR-II OPD achieves a low dark current density of 0.81 nA cm⁻² in photovoltaic mode and shows negligible degradation of the dark current density (Figure 5b), photoresponse (Figure 5c), and response/recovery times (1400 ns/600 ns) after bending for 100 cycles with a curve radius of 9.17 mm (Figure 5d). Further bending 500 times with almost no loss of optoelectronic performance (Figure S11, Supporting Information). All these exceptional electrical and mechanical stabilities of the flexible NIR-II OPD ensure practical applicabil-

ity in wearable vision systems. Figure 5e and Table S9 (Supporting Information) summarize the performance metrics of previously reported flexible OPDs, where our flexible YZ1-based NIR-II OPD demonstrates extremely outstanding performance in terms of responsivity and specific detectivity (Figure S12, Supporting Information).

2.5. Flexible NIR-II OPD Array for Imaging and Identification

To explore the potential applications of the flexible NIR-II OPD, a large-area flexible OPD matrix of 2000 pixels based on the YZ1 NFA was designed and fabricated to mimic the imaging function of biological eyes (Figure 6a and Supporting Information). Each pixel in the matrix features two vertical crossline electrodes with a size of 250 × 250 μm, which can further improve the resolution by designing the bottom and top electrodes more finely. This matrix can operate without the additional integration of switching elements, simplifying the readout circuit, improving array resolution, and reducing overall power consumption. The optimized pixels in the flexible NIR-II OPD matrix exhibit high homogeneity in terms of dark current and photocurrent under illumination (Figure S13, Supporting Information). Benefiting from the inherent flexibility of plastic materials, flexible NIR-II OPD arrays can be tailored to any size and shape to adapt to curved and irregular substrates under bending or torsion for accurate imaging (Figure S14, Supporting Information). By customizing large-area flexible NIR-II OPD arrays to desired shapes, they can be integrated with commercial eyeglass frames to fabricate wearable visual systems for imaging (Figure 6b).

To demonstrate the potential of the flexible NIR-II OPD array for wearable optoelectronics, a YZ1-based NIR-II OPD matrix with 12 × 12 pixels was selected for NIR imaging (more details

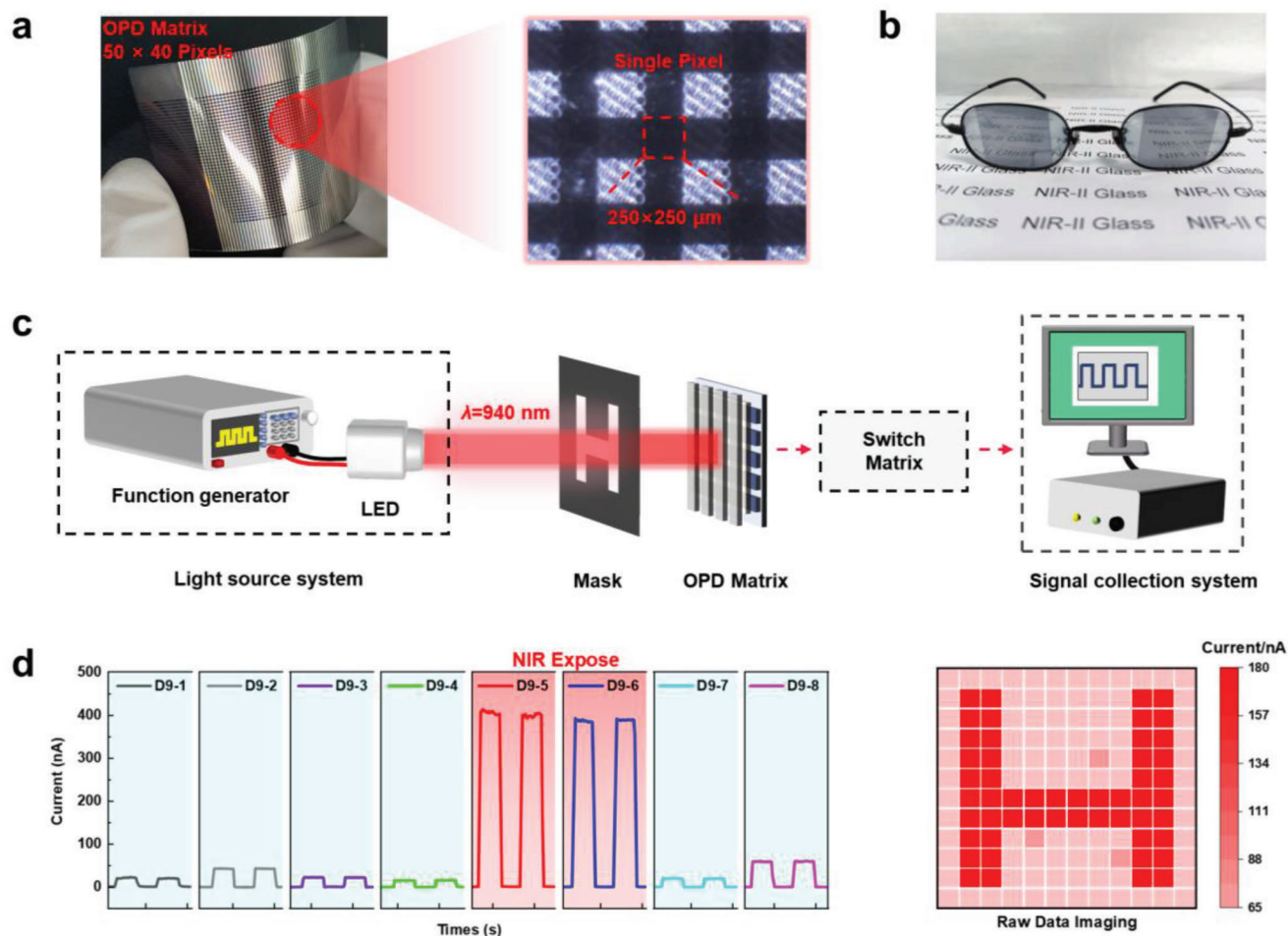


Figure 6. NIR imaging characterizations of flexible NIR-II OPD array. a) Optical image of a flexible YZ1-based NIR-II OPD array and enlarged single pixel. b) Photograph of flexible YZ1-based NIR-II OPD arrays integrated with commercial eyeglass frame. c) Schematic illustration of the flexible YZ1-based NIR-II OPD array for imaging. d) The I - T curves of some YZ1-based NIR-II OPD pixels under 940 nm illumination and the corresponding imaging.

are presented in Figure S15, Supporting Information). As shown in Figure 6c, an image was generated by projecting 940 nm NIR light onto the global large-area flexible OPD array using a shadow mask, where the current of each pixel was recorded by periodically controlling matrix connection switch at 0 V bias voltage. The NIR-II OPD pixels exposed to 940 nm light exhibit clear photoresponse compared to the masked devices (Figure 6d). By visualizing the measured current (Supporting Information), successful imaging of the letter “H” was achieved using the flexible NIR-II OPD array (Figure 6d). Detailed I - T data of each pixel is shown in Figure S16 (Supporting Information). Furthermore, the normal spectral emissivities of alloys are crucial for temperature measurement in metallurgical solidification and plastic processing. As shown in Figure S18 (Supporting Information), the high-temperature NiCr alloy (above 450 °C) emits vis-NIR spectral peaking at 900 nm, and the YZ1-based OPD exhibits a fast and high photoresponse when exposed to the emitted light from the high-temperature NiCr alloy. This suggests the possibility of accurate temperature monitoring and matter identification in practical applications by detecting the emitted light from subjects.

3. Conclusion

In conclusion, we have successfully fabricated a high-sensitivity NIR-II OPD by designing ultranarrow-bandgap NFAs through introducing a highly rigid 2D central unit. The strategic design efficiently mitigates energetic disorder within blend films. More importantly, the introduction of larger and highly electron-deficient end groups effectively broadens the optical absorption spectrum, reduces trap states, and improves charge transport, simultaneously. The optimal YZ1-based device demonstrated exceptional performance over a wide spectrum range from 300 to 1050 nm, including high responsivity (0.27 A W^{-1} at 1000 nm), low dark current density (0.053 nA cm^{-2}), high specific detectivity ($\approx 10^{14}$ Jones), and fast photoresponse (976/600 ns). These performance metrics are comparable to those achieved by popular commercial silicon photodetectors. The impressive results can be attributed to the low trap density, low energetic disorder, and balanced charge mobilities achieved within the photoactive film, primarily owing to the highly rigid backbone of the YZ1 NFA and the well-organized molecular packing in the blend.

Furthermore, by integrating large-area flexible OPD arrays (2000 pixels) with eyeglasses, we have successfully developed a wearable visual system based on high-density OPD arrays for NIR imaging. The proposed artificial visual system represents a significant step toward the next-generation flexible optoelectronics for night imaging, retina prosthesis, machine vision, wellness monitoring, and optical communication.

Supporting Information

Supporting Information is available from the Wiley Online Library or from the author.

Acknowledgements

The authors gratefully acknowledge the financial support from the MoST (2022YFB4200400) and the NSFC (21935007) of China, the National Basic Research Program of China (2022YFA1203304), the Tianjin City (20)CZDJC00740), and the 111 Project (B12015).

Conflict of Interest

The authors declare no conflict of interest.

Data Availability Statement

The data that support the findings of this study are available in the supplementary material of this article.

Keywords

flexible photodetectors, full-spectrum detection, near-infrared imaging, near-infrared organic photodetectors, ultranarrow bandgap non-fullerene acceptors

Received: July 1, 2023

Revised: July 26, 2023

Published online:

- [1] L. Gu, S. Poddar, Y. Lin, Z. Long, D. Zhang, Q. Zhang, L. Shu, X. Qiu, M. Kam, A. Javey, Z. Fan, *Nature* **2020**, 581, 278.
- [2] D. C. D. Pockock, *Trans. Inst. Br. Geogr.* **1981**, 6, 385.
- [3] F. Liao, Z. Zhou, B. J. Kim, J. Chen, J. Wang, T. Wan, Y. Zhou, A. T. Hoang, C. Wang, J. Kang, J.-H. Ahn, Y. Chai, *Nat. Electron.* **2022**, 5, 84.
- [4] H. C. Ko, M. P. Stoykovich, J. Song, V. Malyarchuk, W. M. Choi, C. J. Yu, J. B. Geddes, J. Xiao, S. Wang, Y. Huang, J. A. Rogers, *Nature* **2008**, 454, 748.
- [5] L. Ferlauto, M. J. I. Airaghi Leccardi, N. A. L. Chenais, S. C. A. Gilliéron, P. Vagni, M. Bevilacqua, T. J. Wolfensberger, K. Sivula, D. Ghezzi, *Nat. Commun.* **2018**, 9, 992.
- [6] K. Sim, S. Chen, Z. Li, Z. Rao, J. Liu, Y. Lu, S. Jang, F. Ershad, J. Chen, J. Xiao, C. Yu, *Nat. Electron.* **2019**, 2, 471.
- [7] C. Choi, M. K. Choi, S. Liu, M. Kim, O. K. Park, C. Im, J. Kim, X. Qin, G. J. Lee, K. W. Cho, M. Kim, E. Joh, J. Lee, D. Son, S.-H. Kwon, N. L. Jeon, Y. M. Song, N. Lu, D.-H. Kim, *Nat. Commun.* **2017**, 8, 1664.

- [8] Z. Ge, N. Xu, Y. Zhu, K. Zhao, Y. Ma, G. Li, Y. Chen, *ACS Photonics* **2022**, 9, 59.
- [9] J. Huang, J. Lee, J. Vollbrecht, V. V. Brus, A. L. Dixon, D. X. Cao, Z. Zhu, Z. Du, H. Wang, K. Cho, G. C. Bazan, T.-Q. Nguyen, *Adv. Mater.* **2020**, 32, 1906027.
- [10] S. Park, K. Fukuda, M. Wang, C. Lee, T. Yokota, H. Jin, H. Jinno, H. Kimura, P. Zalar, N. Matsuhisa, S. Umezumi, G. C. Bazan, T. Someya, *Adv. Mater.* **2018**, 30, 1802359.
- [11] Z. Wang, R. Yu, X. Wen, Y. Liu, C. Pan, W. Wu, Z. L. Wang, *ACS Nano* **2014**, 8, 12866.
- [12] R. H. Dycck, G. P. Weckler, *IEEE Trans. Electron Devices* **1968**, 15, 196.
- [13] J. Michel, J. Liu, L. C. Kimerling, *Nat. Photonics* **2010**, 4, 527.
- [14] Y. Song, Z. Zhong, P. He, G. Yu, Q. Xue, L. Lan, F. Huang, *Adv. Mater.* **2022**, 34, 2201827.
- [15] C. Fuentes-Hernandez, W.-F. Chou, T. M. Khan, L. Diniz, J. Lukens, F. A. Larrain, V. A. Rodriguez-Toro, B. Kippelen, *Science* **2020**, 370, 698.
- [16] X. Gong, M. Tong, Y. Xia, W. Cai, J. S. Moon, Y. Cao, G. Yu, C.-L. Shieh, B. Nilsson, A. J. Heeger, *Science* **2009**, 325, 1665.
- [17] T. Someya, M. Amagai, *Nat. Biotechnol.* **2019**, 37, 382.
- [18] T. Yokota, K. Fukuda, T. Someya, *Adv. Mater.* **2021**, 33, 2004416.
- [19] D. Yang, D. Ma, *Adv. Opt. Mater.* **2019**, 7, 1800522.
- [20] X. Wan, C. Li, M. Zhang, Y. Chen, *Chem. Soc. Rev.* **2020**, 49, 2828.
- [21] Y. Chen, Y. Zheng, Y. Jiang, H. Fan, X. Zhu, *J. Am. Chem. Soc.* **2021**, 143, 4281.
- [22] W. Li, Y. Xu, X. Meng, Z. Xiao, R. Li, L. Jiang, L. Cui, M. Zheng, C. Liu, L. Ding, Q. Lin, *Adv. Funct. Mater.* **2019**, 29, 1808948.
- [23] J. Lee, S.-J. Ko, H. Lee, J. Huang, Z. Zhu, M. Seifrid, J. Vollbrecht, V. V. Brus, A. Karki, H. Wang, K. Cho, T.-Q. Nguyen, G. C. Bazan, *ACS Energy Lett.* **2019**, 4, 1401.
- [24] J. Lee, S.-J. Ko, M. Seifrid, H. Lee, B. R. Luginbuhl, A. Karki, M. Ford, K. Rosenthal, K. Cho, T.-Q. Nguyen, G. C. Bazan, *Adv. Energy Mater.* **2018**, 8, 1801212.
- [25] J. Liu, M. Gao, J. Kim, Z. Zhou, D. S. Chung, H. Yin, L. Ye, *Mater. Today* **2021**, 51, 475.
- [26] G. Simone, M. J. Dyson, C. H. L. Weijtens, S. C. J. Meskers, R. Coehoorn, R. A. J. Janssen, G. H. Gelinck, *Adv. Opt. Mater.* **2020**, 8, 1901568.
- [27] J. Kublitski, A. Hofacker, B. K. Boroujeni, J. Benduhn, V. C. Nikolis, C. Kaiser, D. Spoltore, H. Kleemann, A. Fischer, F. Ellinger, K. Vandewal, K. Leo, *Nat. Commun.* **2021**, 12, 551.
- [28] W. Deng, W. Liu, R. Qian, H. Wu, *J. Phys. Chem. Lett.* **2022**, 13, 544.
- [29] H. Chen, Y. Zou, H. Liang, T. He, X. Xu, Y. Zhang, Z. Ma, J. Wang, M. Zhang, Q. Li, C. Li, G. Long, X. Wan, Z. Yao, Y. Chen, *Sci China Chem* **2022**, 65, 1362.
- [30] H. Chen, H. Liang, Z. Guo, Y. Zhu, Z. Zhang, Z. Li, X. Cao, H. Wang, W. Feng, Y. Zou, L. Meng, X. Xu, B. Kan, C. Li, Z. Yao, X. Wan, Z. Ma, Y. Chen, *Angew. Chem., Int. Ed.* **2022**, 61, e202209580.
- [31] P. Li, X. Meng, K. Jin, Z. Xu, J. Zhang, L. Zhang, C. Niu, F. Tan, C. Yi, Z. Xiao, Y. Feng, G.-W. Wang, L. Ding, *Carbon Energy* **2023**, 5, e250.
- [32] Z. Yao, X. Liao, K. Gao, F. Lin, X. Xu, X. Shi, L. Zuo, F. Liu, Y. Chen, A. K. Y. Jen, *J. Am. Chem. Soc.* **2018**, 140, 2054.
- [33] K. Tvingstedt, C. Deibel, *Adv. Energy Mater.* **2016**, 6, 1502230.
- [34] P. C. Y. Chow, T. Someya, *Adv. Mater.* **2020**, 32, 1902045.
- [35] Z. Wu, N. Li, N. Eedugurala, J. D. Azoulay, D.-S. Leem, T. N. Ng, *Npj Flex Electron* **2020**, 4, 6.
- [36] A. J. M. Van Breemen, R. Olleero, S. Shanmugam, B. Peeters, L. C. J. M. Peters, R. L. van de Ketterij, I. Katsouras, H. B. Akkerman, C. H. Frijters, F. Di Giacomo, S. Veenstra, R. Andriessen, R. A. J. Janssen, E. A. Meulenkaamp, G. H. Gelinck, *Nat. Electron.* **2021**, 4, 818.
- [37] K. Rayner, T. J. Smith, G. L. Malcolm, J. M. Henderson, *Psychol Sci* **2009**, 20, 6.

- [38] H. Ohta, *Smart CMOS Image Sensors and Applications*, CRC Press **2020**.
- [39] X. Ma, H. Bin, B. T. van Gorkom, T. P. A. van der Pol, M. J. Dyson, C. H. L. Weijtens, M. Fattori, S. C. J. Meskers, A. J. J. M. van Breemen, D. Tordera, R. A. J. Janssen, G. H. Gelinck, *Adv. Mater.* **2023**, *35*, 2209598.
- [40] W. Shockley, W. T. Read, *Phys. Rev.* **1952**, *87*, 835.
- [41] M. Kuik, L. J. A. Koster, G. A. H. Wetzelaer, P. W. M. Blom, *Phys Rev Lett* **2011**, *107*, 256805.
- [42] N. Zarrabi, O. J. Sandberg, S. Zeiske, W. Li, D. B. Riley, P. Meredith, A. Armin, *Nat. Commun.* **2020**, *11*, 5567.
- [43] C. t. Sah, R. N. Noyce, W. Shockley, *Proc. IRE* **1957**, *45*, 1228.
- [44] C. Kaiser, O. J. Sandberg, N. Zarrabi, W. Li, P. Meredith, A. Armin, *Nat. Commun.* **2021**, *12*, 3988.
- [45] F. Huang, T. He, M. Li, L. Meng, W. Feng, H. Liang, Y. Zhou, X. Wan, C. Li, G. Long, Z. Yao, Y. Chen, *Chem. Mater.* **2022**, *34*, 6009.